Stable metal anodes enabled by a labile organic molecule bonded to a reduced graphene oxide aerogel

Yue Gao[a], Daiwei Wang[a], Yun Kyung Shin[a], Zhifei Yan[b], Zhuo Han[c], Ke Wang[a], Md Jamil Hossain[a], Shuling Shen[c], Atif AlZahrani[a], Adri C. T. van Duin[a], Thomas E. Mallouk[b], and Donghai Wang[a,1]

[a]Department of Mechanical Engineering, The Pennsylvania State University, University Park, PA 16802; [b]Department of Chemistry, University of Pennsylvania, Philadelphia, PA 19104; and [c]School of Materials Science and Engineering, University of Shanghai for Science and Technology, Shanghai 200093, China

Edited by Catherine J. Murphy, University of Illinois at Urbana–Champaign, Urbana, IL, and approved October 13, 2020 (received for review February 1, 2020)

Metallic anodes (lithium, sodium, and zinc) are attractive for rechargeable battery technologies but are plagued by an unfavorable metal–electrolyte interface that leads to nonuniform metal deposition and an unstable solid–electrolyte interphase (SEI). Here we report the use of electrochemically labile molecules to regulate the electrochemical interface and guide even lithium deposition and a stable SEI. The molecule, benzenesulfonyl fluoride, was bonded to the surface of a reduced graphene oxide aerogel. During metal deposition, this labile molecule not only generates a metal-coordinating benzenesulfonate anion that guides homogeneous metal deposition but also contributes lithium fluoride to the SEI to improve Li surface passivation. Consequently, high-efficiency lithium deposition with a low nucleation overpotential was achieved at a high current density of 6.0 mA cm^{-2}. A Li|$LiCoO_2$ cell had a capacity retention of 85.3% after 400 cycles, and the cell also tolerated low-temperature (−10 °C) operation without additional capacity fading. This strategy was applied to sodium and zinc anodes as well.

electrochemical interface | solid–electrolyte interphase | metallic anodes | functionalized reduced graphene oxide

Rechargeable batteries based on metal anodes including lithium (Li), sodium (Na), and zinc (Zn) show great promise in achieving high energy density (1–3). Unfortunately, the electrochemical interface of the metal anodes is not favorable for metal deposition. Metal nucleation is inhomogeneous at the surface, leading to the growth of metal dendrites (4–7) and the formation of an unstable solid–electrolyte interphase (SEI) that is incapable of protecting metals from the side reactions with the electrolyte (8–12).

Substantial efforts have been devoted to stabilizing the interface of metal anodes, especially for Li metal. These include the design of artificial protective layers (13–17), alternative electrolytes (18–24), and sacrificial additives (25–30) to stabilize the metal–electrolyte interface, the development of mechanically robust coatings (31–34) to block Li dendrite growth, and the use of structured scaffolds to host dendrite-free Li deposition by reducing local current densities (35–43). However, the performance of metal anodes remains poor under high-current or low-temperature conditions. This is because the inhomogeneous Li nucleation and unstable SEI problems have not been well addressed, and these problems at the interface are even exacerbated under critical operating conditions, especially high-current densities and low temperatures (5, 6, 44).

Toward this end, we report a simple molecular approach for regulating the electrochemical interface of metal anodes, which enables even Li deposition and stable SEI formation in a conventional electrolyte. This was realized by bonding a labile organic molecule, benzenesulfonyl fluoride (BSF), to a reduced graphene oxide (rGO) aerogel surface as the Li anode host (Fig. 1*A*). During Li deposition, BSF molecules electrochemically decompose at the interface and generate benzenesulfonate anions bonded to the rGO aerogel (Fig. 1*B*). The conjugated anions have a strong binding affinity for Li, serving as lithiophilic sites on the rGO surface to synergistically induce homogeneous Li nucleation of Li on the rGO surface. At the same time, BSF molecules contribute LiF to the SEI layer, which facilitates Li surface passivation (Fig. 1*C*). As a result, high-efficiency (99.2%) Li deposition was achieved at a Li deposition amount of 6.0 mAh cm^{-2} and a current density of 6.0 mA cm^{-2}; the barrier to Li nucleation was markedly reduced, as evidenced by the low nucleation overpotentials at high-current density (6.0 mA cm^{-2}) or at a low temperature (−10 °C). A 400-cycle life with a capacity retention of 83.6% was achieved for a Li|$LiCoO_2$ (LCO) cell in a conventional carbonate electrolyte. Moreover, with the organic molecule-tuned interface, the Li|LCO cell can be stably cycled at a low operating temperature (−10 °C). This approach was applied to Na and Zn metal anodes as well.

Results and Discussion

Li Nucleation Regulated by BSF-rGO Aerogel. The key to achieving stable Li deposition is to have a Li-binding surface for homogeneous Li nucleation. We thus screened a variety of conjugated organic molecules as preferred Li nucleation sites, including benzenesulfonate, phenolate, nitrobenzene, pyridine, and benzene (Fig. 2*A*). These molecules were bonded to the surface, defects, and edge sites of an rGO aerogel (45) via an electron-transfer reaction with diazonium salts (*SI Appendix*, Figs. S1–S6) (46, 47). We compared the Li binding energy and Li nucleation overpotential of the organic molecule-functionalized rGO aerogel hosts. By using a

Significance

Rechargeable batteries based on metal anodes are highly desirable due to their high energy density. However, the electrochemical interface is generally not favorable for metal deposition, resulting in dendritic metal growth and an unstable solid–electrolyte interphase (SEI). We altered the interface using a labile organic molecule, benzenesulfonyl fluoride. This molecule was bonded to the surface of a reduced graphene oxide aerogel, which not only guides uniform metal deposition but also enables formation of a stable SEI layer. The lithium metal batteries showed stable cycling and excellent tolerance to low-temperature operation. Stable sodium and zinc anodes were also realized, demonstrating the versatility of this concept.

Author contributions: Y.G., A.C.T.v.D., T.E.M., and Donghai Wang designed research; Y.G., Daiwei Wang, Y.K.S., Z.Y., Z.H., K.W., M.J.H., S.S., and A.A. performed research; Y.G., Daiwei Wang, K.W., A.C.T.v.D., T.E.M., and Donghai Wang analyzed data; and Y.G., T.E.M., and Donghai Wang wrote the paper.

The authors declare no competing interest.

This article is a PNAS Direct Submission.

[1]To whom correspondence may be addressed. Email: dwang@psu.edu.

This article contains supporting information online at https://www.pnas.org/lookup/suppl/doi:10.1073/pnas.2001837117/-/DCSupplemental.

First published November 16, 2020.

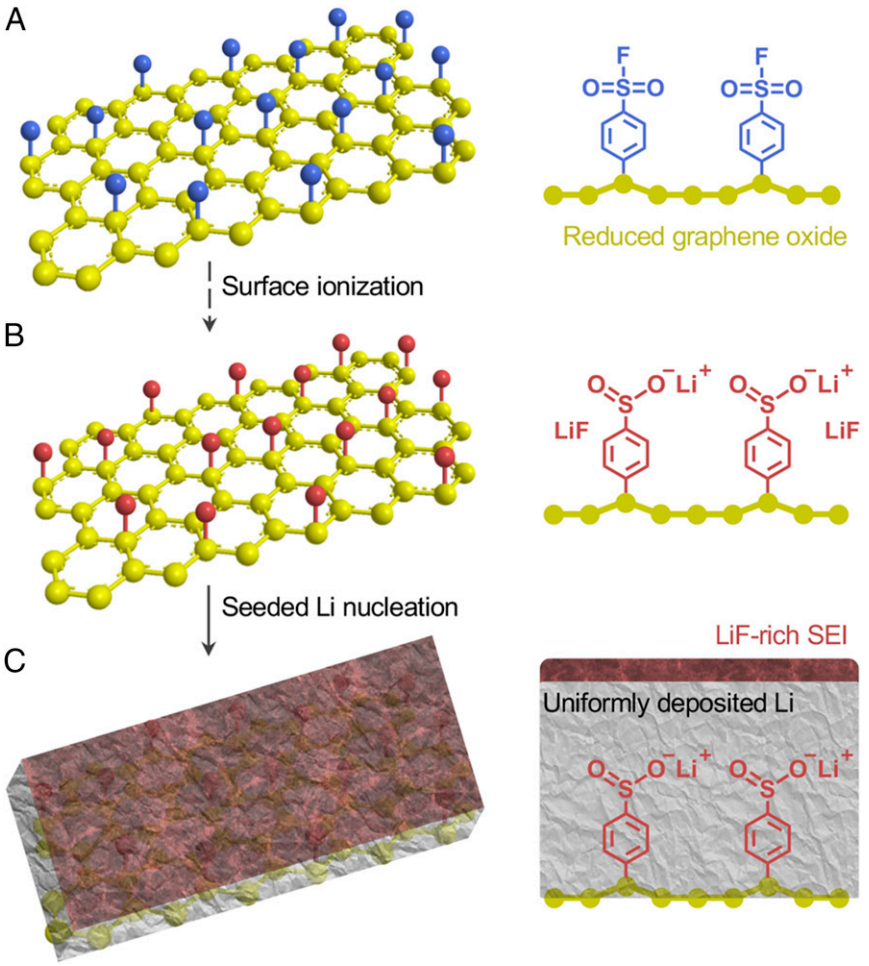

Fig. 1. Illustration of a stable interface for Li deposition using a labile organic molecule, benzenesulfonyl fluoride (BSF). (*A*) Covalently bonded BSF on the rGO aerogel surface. (*B*) In situ generation of a lithiophilic conjugated anion (benzenesulfonate) and LiF on the surface during Li deposition. (*C*) Li nucleation preferentially occurs at the conjugated anion sites owing to the strong Li binding affinity, which leads to uniform Li deposition. In addition, the LiF that is formed is in the SEI layer and passivates the Li surface.

density-functional theory (DFT) simulation, the BSF-derived anion, benzenesulfonate, was calculated to have a high Li binding energy of −3.79 eV, superior to that of the bare graphene layer (−1.84 eV) and other candidate molecules (Fig. 2*B* and *SI Appendix*, Figs. S7–S11). Consistently, a low Li nucleation overpotential of ∼20 mV on the BSF-rGO aerogel was recorded, which is much lower than the ∼72 mV found with the bare rGO aerogel and other molecules (Fig. 2*C* and *SI Appendix*, Fig. S12). Fig. 2*D* shows the voltage profiles of Li deposition on the BSF-rGO aerogel and on the bare rGO aerogel. An electrolyte consisting of 1 M lithium hexafluorophosphate ($LiPF_6$) in ethylene carbonate (EC)/ethyl methyl carbonate (EMC) was used. At a high-current density (6.0 mA cm^{-2}), the barrier to Li deposition in the control cell increased progressively, as evidenced by the higher Li nucleation overpotential of ∼101 mV. When the temperature falls to −10 °C, the overpotential grew to ∼193 mV due to slower kinetics (48, 49). In stark contrast, BSF-regulated Li nucleation had much lower overpotentials of ∼33 mV at 25 °C and ∼121 mV at −10 °C, which suggests the effective regulation of Li deposition.

Stable SEI Enabled by the BSF-rGO Aerogel. In addition to regulating Li nucleation, BSF molecules also contribute LiF to the SEI layer. We first investigated the electrochemical activity of BSF-rGO aerogel by cyclic voltammetry. The SEI formation peak of the bare rGO aerogel was observed from 0.25 to −0.1 V vs. Li/Li^+ (Fig. 3*A*). For the BSF-rGO aerogel, the peak shifted positively by ∼0.17 V, indicating that BSF is involved in SEI formation and BSF decomposition occurs before that of the electrolyte. We analyzed the decomposition products by NMR and X-ray photoelectron spectroscopy (XPS). The BSF-rGO aerogel electrode was scanned from 1.5 to 0.05 V over two cycles at 1 mV s^{-1}; 0.5 M lithium bis(oxalate)borate (LiBOB) in EC/EMC electrolyte was used to exclude the generation of F-containing species. In the decomposition products, we found LiF in the ^{19}F NMR spectrum (Fig. 3*B*) and observed both LiF and benzenesulfonate (C_6H_5-SO_2-) in the XPS spectra (*SI Appendix*, Fig. S13). These findings support the hypothesis that BSF molecules can decompose and generate LiF and benzenesulfonate during the Li deposition.

We studied the nanostructure of formed SEI by using cryogenic transmission electron spectroscopy (cryo-TEM). Fig. 4*A* shows a TEM image of the interface of a BSF-rGO aerogel@Li electrode. The SEI is homogeneous, and consists of an amorphous layer containing predominantly LiF nanocrystals and a small amount of Li_2CO_3 and Li_2O nanocrystals. We confirmed the lattice spacings in corresponding fast Fourier transform images (*SI Appendix*, Fig. S14). In contrast, the SEI on the bare

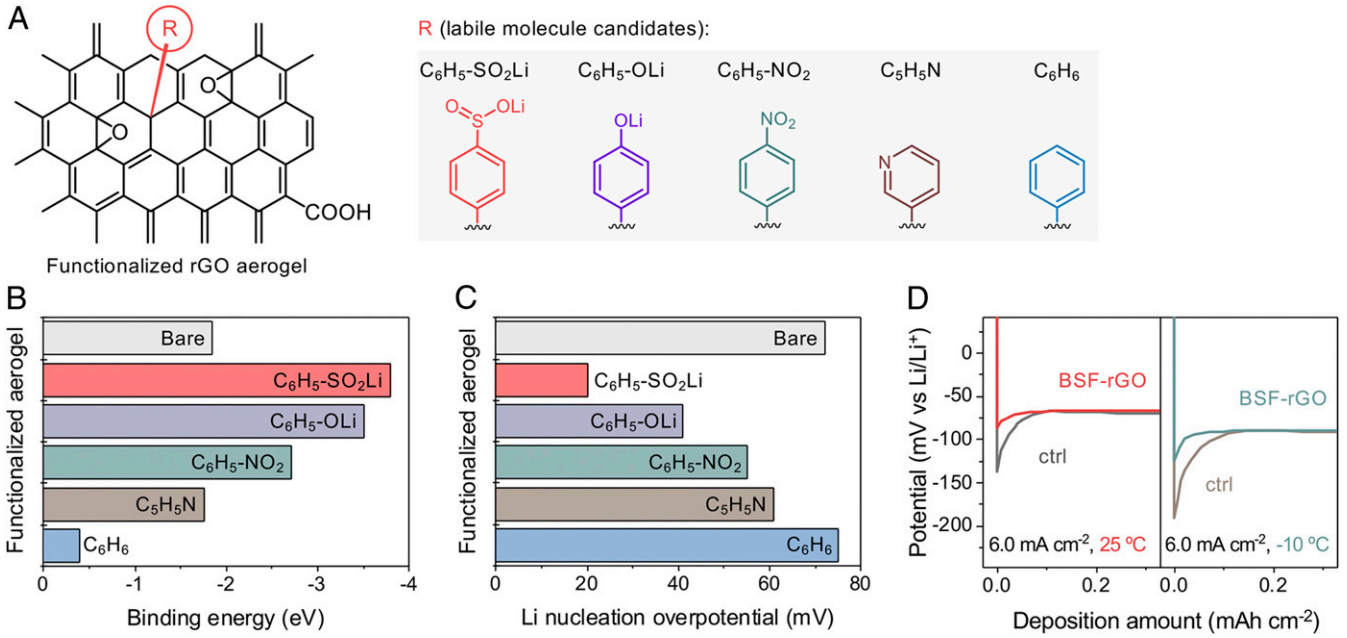

Fig. 2. Functionalization of the rGO aerogel surface by conjugated molecules for stabilizing the Li-electrolyte interface. (*A*) Idealized structures of the functionalized rGO aerogels. The labile molecules (R) can be bonded on the surface, defects, and edges of the rGO aerogels. (*B*) Comparison of the binding energy for Li atoms on the functionalized graphene layers, calculated by DFT simulation. (*C*) Comparison of Li nucleation overpotential on the functionalized rGO aerogels at a high current density of 6 mA cm^{-2}. (*D*) Voltage profiles of Li nucleation on the BSF-rGO aerogel surface at 25° and -10 °C, respectively. A 1 M $LiPF_6$ in EC/EMC electrolyte was used.

rGO aerogel@Li electrode is highly heterogeneous, in which we primarily observed Li_2CO_3 and Li_2O nanocrystals (Fig. 4*B* and *SI Appendix*, Fig. S15). We performed energy-loss spectroscopy (EELS) to further study the composition of the SEI. The Li K-edge spectrum taken from the TEM image of the SEI on the BSF-rGO aerogel@Li electrode shows a LiF-dominant spectral features, as evidenced by a peak at ∼62 eV (50) (Fig. 4*C*). Contrastingly, the peak shape of the control SEI mainly corresponds to Li_2CO_3 and Li_2O. The regions taken for EELS measurements are shown in *SI Appendix*, Figs. S14*E* and S15*E*.

We further elucidated SEI composition by conducting XPS on the rGO aerogel electrodes after 50 cycles in a 1 M $LiPF_6$ in EC/EMC electrolyte. As depicted in Fig. 4*D*, the SEI of the bare rGO aerogel@Li electrode mainly consists of Li-CO_2- salts (peaks at 56.2 eV in the Li 1s spectrum and 289.1 eV in the C 1s spectrum), Li-O- species (the peak at 54.5 eV in the Li 1s spectrum), LiF salts (peaks at 684.6 eV in the F 1s spectrum and 57.6 eV in the Li 1s spectrum), $P_xF_yO_z^-$ species [the peak at 686.2 eV in the F 1s spectrum and 136.7 eV in the P 2p spectrum (*SI Appendix*, Fig. S16*A*)] (51), and organic species including C-C (the peak at 284.6 eV in the C 1s spectrum) and C-O (the peak at 286.2 eV in the C 1s spectrum). By calculating all of the Li salt concentrations in the SEI, we determined that the dominant salt of the conventional SEI is Li-CO_2- (45 at. %), and the LiF concentration is only 21 at. % (Fig. 4*E*). The SEI on the BSF-rGO aerogel contains a higher concentration of LiF (45 at. %) and a lower concentration of Li-CO_2- (36%), verifying that LiF is added by decomposition of BSF (Fig. 4*F*). Meanwhile, the Li-CO_2- content in all of the C-containing species is very low, suggesting that formation of Li-CO_2- by the electrolyte is substantially suppressed (Fig. 4*G* and *SI Appendix*, Fig. S16*B*). Moreover, by using XPS depth profiling, we found that the SEI on the BSF-rGO aerogel has no discernible thickness increase with cycling, implying its excellent stability (*SI Appendix*, Fig. S17 *A* and *B*). This is in sharp contrast to the marked thickness increase of the control SEI (*SI Appendix*, Fig. S17 *C* and *D*).

Uniform Li Deposition on the BSF-rGO Aerogel. We next probed the morphology of BSF-regulated Li deposition at a current density of 6.0 mA cm^{-2} by scanning electron microscopy (SEM). The pristine BSF-rGO aerogel has interconnected macropore channels (Fig. 5 *A* and *B*), a specific surface area of ∼300 m^2 g^{-1}, and void space of ∼96.6 vol. %. Fig. 5 *C* and *D* show the top-view images of the BSF-rGO aerogel that accommodates 6.0 mAh cm^{-2} Li and after 50 cycles at 25 °C. Li grew uniformly on the BSF-rGO aerogel in a dendrite-free way. The electrode thicknesses before and after the Li deposition were ∼100 and 106 μm, respectively, showing no discernible increase (*SI Appendix*, Fig. S18). In contrast, the Li deposition on the bare rGO aerogel is not as uniform as the BSF-rGO aerogel, as evidenced by the growth of Li metal with a particle-shaped morphology (Fig. 5*E* and *SI Appendix*, Fig. S19 *A* and *B*). Dendrite-free Li deposition was also realized

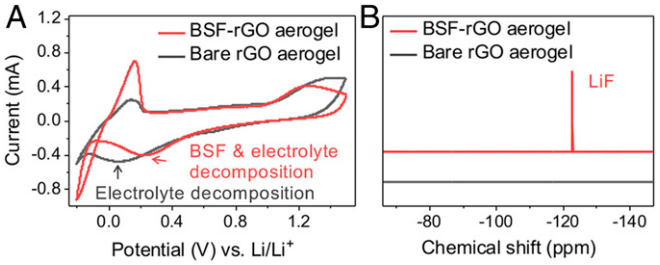

Fig. 3. Electrochemical activity of the BSF on the rGO aerogel. (*A*) Cyclic voltammogram of the BSF-rGO aerogel and bare rGO aerogel electrodes. The scan rate is 10 mV s^{-1}. (*B*) ^{19}F NMR spectra of SEI formed on the BSF-rGO aerogel and rGO aerogel in a 0.5 M LiBOB in EC/EMC electrolyte. LiF was exclusively found in the BSF-rGO aerogel sample.

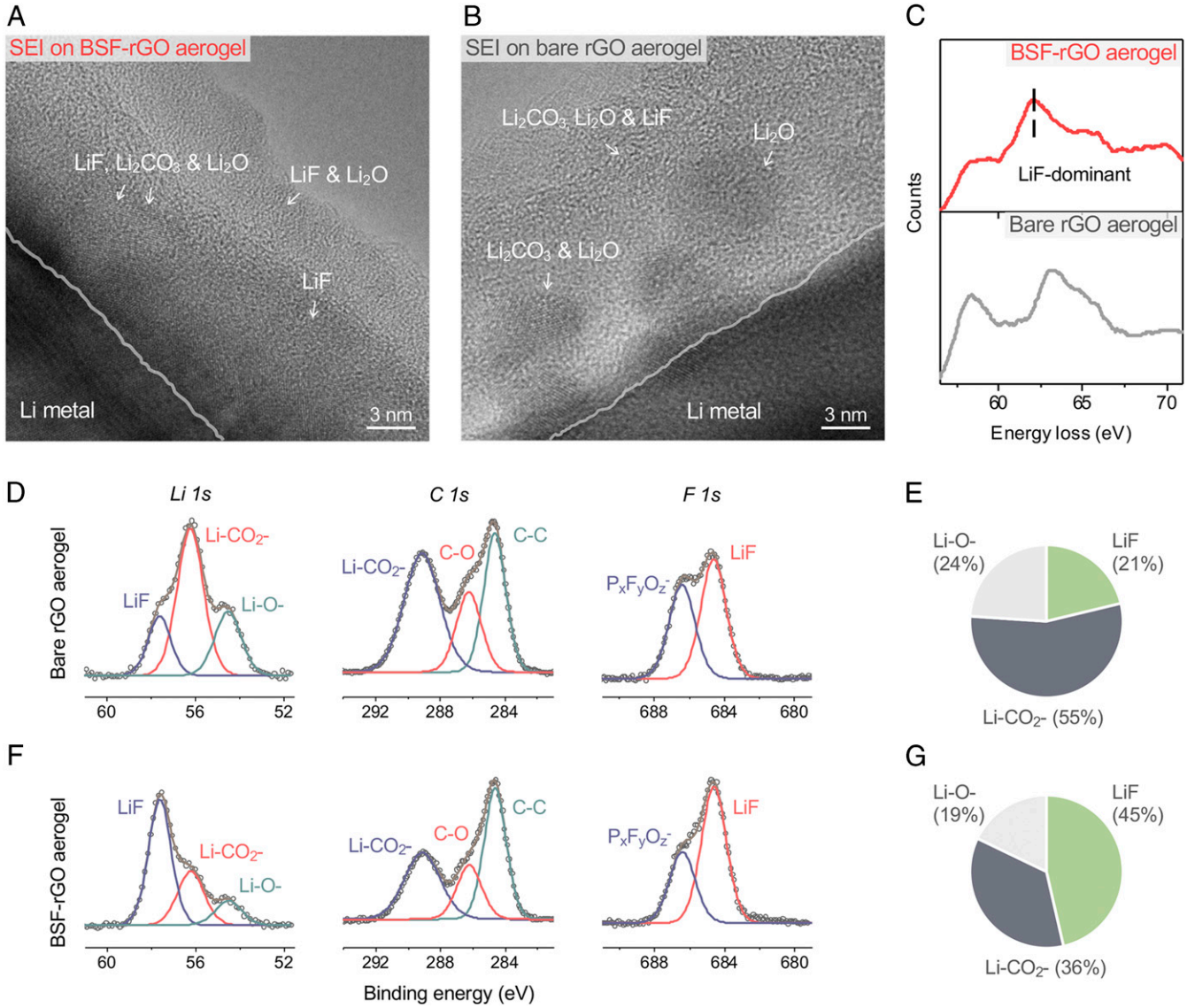

Fig. 4. Structure and composition of the SEI on the BSF-rGO aerogel@Li electrode. (*A*–*C*) TEM images of the SEI layers that formed on the BSF-rGO aerogel@Li (*A*) and bare rGO aerogel@Li (*B*) after 10 cycles and the Li K-edge spectra corresponding to the SEI layers (*C*). (*D*) XPS spectra of the SEI of a BSF-rGO aerogel@Li electrode. (*E*) Concentrations of Li salts in the BSF-rGO aerogel@Li SEI. (*F*) XPS spectra of the SEI of a bare rGO aerogel@Li electrode. (*G*) Concentrations of Li salts in the bare rGO aerogel@Li SEI. The use of BSF-rGO aerogel substantially increases the concentration of LiF in the SEI layer. The electrodes were cycled in a 1 M $LiPF_6$ in EC/EMC electrolyte for 50 cycles.

when Li deposition amounts were 12 and 16 mAh cm^{-2} (*SI Appendix*, Fig. S20). In addition, we performed Li deposition at −10 °C, at which Li dendrite growth is typically intensified (52). Encouragingly, we observed uniform Li deposition on the BSF-rGO aerogel (Fig. 5 *F* and *G*). Contrastingly, we found Li metal with a particle-shaped morphology on the bare rGO aerogel (Fig. 5*H* and *SI Appendix*, Fig. S19 *C* and *D*). Based on these findings, we concluded that the use of the BSF molecule and rGO aerogel synergistically induces highly uniform and dendrite-free Li deposition.

Stable Cycling of BSF-rGO Aerogel@Li Anodes. We studied the electrochemical performance of BSF-rGO aerogel@Li anodes. The Li deposition stability was monitored by the evolution of impedance in a symmetric Li|Li cell, which was cycled at −10 °C using a 1 M $LiPF_6$ in EC/EMC with lithium nitrate ($LiNO_3$) (0.4%) and LiBOB (2%) electrolyte. The overall interfacial impedance of the cell incorporating BSF-rGO aerogel increased from 102 to 225 Ω from the 50th to the 200th cycle, while that of the bare rGO aerogel increased from 216 to 422 Ω (Fig. 6*A* and *SI Appendix*, Fig. S21). The limited impedance increase is attributed to suppressed SEI reformation. The Coulombic efficiency of Li deposition was measured in a Li|BSF- rGO aerogel cell at a deposition amount of 6.0 mAh cm^{-2} and a current density of 6.0 mA cm^{-2}. An average Coulombic efficiency of 99.2% was measured in 400 cycles (Fig. 6*B*), in contrast to fluctuating efficiencies with the bare rGO aerogel. When higher Li deposition amounts of 8.0 and 12.0 mAh cm^{-2} were applied, the average efficiencies reached 99.1% and 89.8%, respectively (*SI Appendix*, Fig. S22).

We next studied the cycling stability of Li metal batteries. LCO cathodes with a capacity of 2.3 mAh cm^{-2} were predelithiated and paired with BSF-rGO aerogel@Li anodes with 12.0 mAh cm^{-2} of Li. 1 M $LiPF_6$ in EC/EMC with $LiNO_3$ and

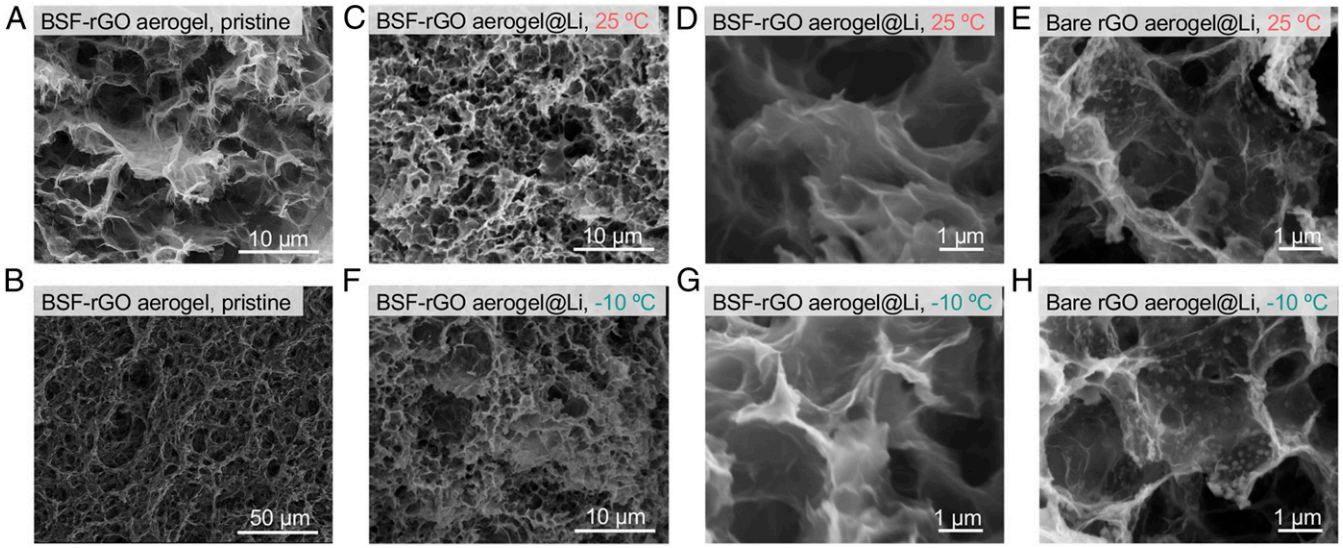

Fig. 5. Morphology of Li deposition on the BSF-rGO aerogel at 25 and -10 °C, respectively. (*A* and *B*) SEM images of a pristine BSF-rGO aerogel before cycling. (*C* and *D*) SEM images of a cycled BSF-rGO aerogel@Li electrode at 25 °C. (*E*) An SEM image of a cycled bare rGO aerogel@Li electrode at 25 °C. (*F* and *G*) SEM images of a cycled BSF-rGO aerogel@Li electrode at −10 °C. (*H*) An SEM image of a cycled bare rGO aerogel@Li electrode at −10 °C. The electrodes were collected after 50 cycles with a Li deposition amount of 6.0 mAh cm^{-2} at a current density of 6.0 mA cm^{-2}.

LiBOB electrolyte was used. The cell incorporating a BSF-rGO aerogel@Li anode had a capacity retention of 83.6% over 400 cycles (Fig. 6*C*) and presented stable voltage profiles upon cycling (*SI Appendix*, Fig. S23*A*). In contrast, a control cell incorporating a bare rGO aerogel@Li anode showed a capacity retention of only 50% after 240 cycles with severe cell polarization (*SI Appendix*, Fig. S23*B*). Following these experiments, we also intentionally aged the Li|LCO cells at low temperatures, in order to further examine the stability of the Li anode under harsh conditions. The cells were first cycled at −10 and 0 °C for 25 cycles, respectively, and then constantly cycled at 25 °C. As expected, with the low-temperature aging process, the cycle life of the Li|LCO cell was markedly shortened. The control cell showed progressive capacity fading (Fig. 6*D* and *SI Appendix*, Fig. S24*A*), with a 50% capacity retention after 173 cycles. In contrast, with the BSF-rGO aerogel@Li anode, the cell had a capacity retention of 85.3% after 400 cycles (Fig. 6*D*) and showed stable voltage profiles (*SI Appendix*, Fig. S24*B*). We further cycled the cell alternately at 25 and 0 °C (Fig. 6*E*); the cell performance was also comparable to that cycled at 25 °C (Fig. 6*C*). Besides, Li|LCO cells with areal capacities of 3.1 and 1.0 mAh cm^{-2} delivered 200-cycle and 700-cycle lives, respectively (*SI Appendix*, Figs. S25 and S26). These experiments clearly show that the use of the BSF-rGO aerogel provides stable electrodeposition and a stabilized SEI for Li metal anodes.

In addition, we applied this approach for Na and Zn metal anodes. By analogy to its reactions at the Li surface, BSF generates benzenesulfonate and NaF (*SI Appendix*, Fig. S27)/ZnF_2 (*SI Appendix*, Fig. S28) on the Na and Zn metal surfaces, respectively. Na and Zn deposition also showed high efficiencies (*SI Appendix*, Figs. S29 and S30) and low nucleation overpotentials (*SI Appendix*, Figs. S31 and S32).

Conclusions

We have demonstrated a chemical approach to stabilizing the interface of Li metal anodes under high-current-density conditions. This was realized by bonding a labile organic molecule to an rGO aerogel surface. The resulting surface not only guides uniform Li deposition via Li-binding surface sites but also passivates the Li surface by producing additional LiF in the SEI. The use of BSF markedly reduced Li nucleation overpotentials at high-current density (6 mA cm^{-2}) and under low-temperature (−10 °C) conditions. The Li|$LiCoO_2$ cells had long cycle lives in the conventional carbonate electrolyte and were able to tolerate low-temperature operations. This approach was also applied to Na and Zn metal anodes.

Materials and Methods

Synthesis of the BSF-rGO Aerogels. The rGO aerogels were prepared by a hydrothermal synthesis approach. In general, we sealed an aqueous solution of graphene oxide (2 mg ml^{-1}) in a Teflon-lined autoclave reactor and then hydrothermally heated it at 180 °C for 20 h. After cooling to room temperature, the rGO hydrogel was obtained and was immediately hydrothermally treated with an aqueous solution of ammonia (14 vol/vol %) at 90 °C for 1 h. The resulting rGO aerogel was then dried by using a free dryer at −45 °C and in a vacuum oven at 100 °C. To perform the modification reaction of rGO aerogels, the dried rGO aerogels were immersed in a solution of 50 mmol (4-fluorosulfonyl)benezenediazonium tetrafluoroborate and 0.1 mol tetrabutylammonium hexafluorophosphate in degassed acetonitrile under an argon atmosphere. The reaction was carried out at room temperature in the absence of light for 36 h. The product was rinsed with acetonitrile six times, immersed in acetonitrile overnight, and dried in a vacuum chamber at 100 °C before use.

Sample Preparations for NMR and XPS Measurements. Samples for ^{19}F NMR tests were prepared by immersing the cycled BSF-rGO and rGO electrodes in 1.5 mL D_2O for 1 h. The solution was centrifuged and the supernatant was used for NMR experiments. To perform XPS measurement, electrode samples were rinsed with EMC two times, dried in a vacuum chamber, and immediately transferred to the instrument by using an air-controlled vessel filled with argon gas.

Electrochemical Testing. Electrochemical tests of battery cells were conducted on Landt battery testers using CR 2016 coin cells under galvanostatic charge–discharge conditions at different currents. To measure the Coulombic efficiency of metal deposition, we predeposited 6.0 mAh cm^{-2} Li in the BSF-

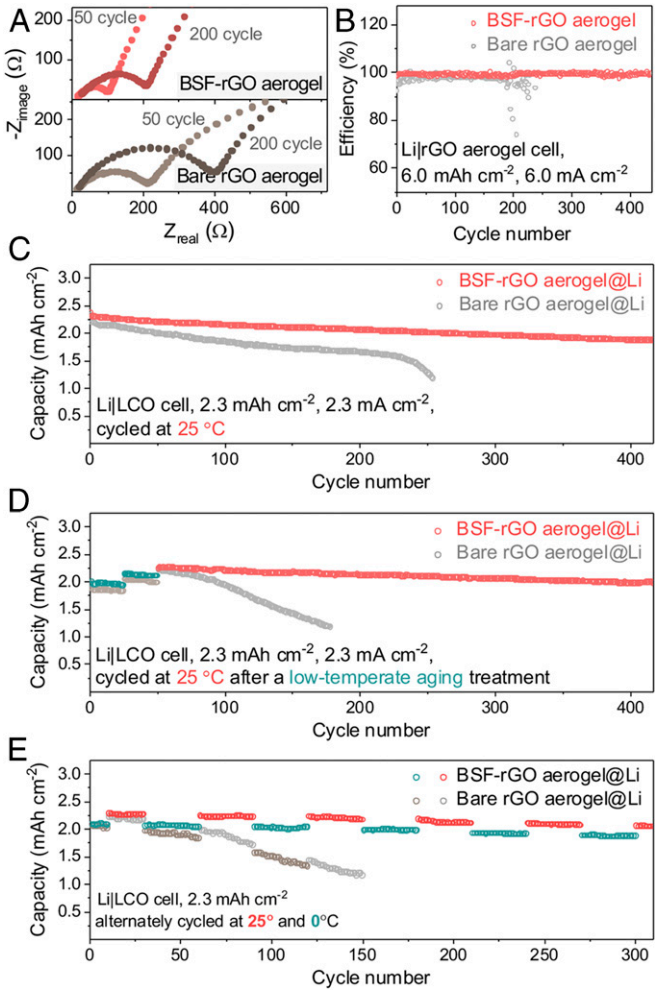

Fig. 6. Electrochemical performance of BSF-rGO aerogel@Li anodes. (*A*) Time-dependent Nyquist plots showing the evolution of impedance of Li|Li cells at −10 °C. (*B*) Coulombic efficiency of Li deposition in the Li|rGO aerogel cells with a deposition amount of 6.0 mAh cm^{-2}. (*C*) Cycling stability of Li|LCO cells constantly cycled at 25 °C. (*D*) Cycling stability of Li|LCO cells that were firstly cycled at -10° and 0 °C for 25 cycles, respectively, and then cycled at 25 °C. (*E*) Cycling stability of Li|LCO cells that were cycled at 25° and 0 °C alternately.

rGO aerogel electrode and measured the amount of stripped Li to calculate Coulombic efficiency. The counter Li electrode was replaced with fresh Li after every 100 cycles due to Li dendrite growth on its surface. To prepare the Li|LCO cells, LCO cathodes were fabricated by mixing LCO powders, conductive carbon, and polyvinylidene fluoride binder at a mass ratio of 85:5:10 in anhydrous *N*-methyl-2-pyrrolidone. The slurry was cast onto Al foil, and the electrode was dried in a vacuum chamber. LCO cathodes were predelithiated to 4.2 V at a current density of 0.2 mA cm^{-2} and then paired with the BSF-rGO aerogel@Li anodes. This treatment helps exclude the gassing issue caused by the SEI formation of 4-V cathode material.

Cryo-TEM Experiments. TEM samples were fabricated by using an "in situ lift-out" technique with an FEI Helios Nanolab 660 Dual Beam focused ion beam. The prepared samples were quickly transferred to a cryo-TEM holder and inserted into the microscope. TEM images were captured on a dual spherical aberration-corrected FEI Titan2 G2 60–300 STEM at an accelerating voltage of 300 kV. EELS spectral imaging was performed using a Gatan GIF Quantum ERS 966 system.

DFT Calculation of Li Binding Energy. For the calculation of the binding energy of Li metals on graphene and the BSF-graphene layer, spin-polarized first-principles DFT calculations were performed using the Vienna ab initio simulation package (53) with the plane-wave basis sets. The DFT calculations used projector augmented-wave (54) pseudopotentials and Perdew-Burke-Ernzerhof (55) exchange-correlation functional with an energy cutoff of 600 eV. For an estimate of the dispersion interactions, the Grimme's DFT dispersion correction (DFT-D3) was used (56). The model graphene layer consists of 72 carbon atoms with hydrogen-capped zigzag edges. The lattice constant of a primitive unit cell of graphene in this calculation is 2.46 Å. The adatom graphene was modeled by adding one metal atom to the hollow, top or edge sites on the graphene surface, which corresponds to a coverage of 1 adatom per 72 C atoms. The BSF-graphene was generated by adding one benzenesulfonyl group to the top site of the graphene surface. The Brillouin zone was sampled with a $4 \times 1 \times 4$ Γ-centered k-point mesh and Gaussian smearing with a width of $\sigma = 0.2$ eV used for the occupancies of the electronic levels. For each binding site of the adatom graphene and the BSF-graphene, the ionic coordinates of all atoms were relaxed in all directions. For the top site, which is set directly above a carbon atom, the metal atom is relaxed along the z direction while remaining fixed in the x- and y directions.

Data Availability. All study data are included in the article and *SI Appendix*.

ACKNOWLEDGMENTS. This work was supported by the Assistant Secretary for Energy Efficiency and Renewable Energy, Office of Vehicle Technologies of the US Department of Energy, through the Advanced Battery Materials Research Program (Battery500 Consortium) Award DE-EE0008198. Z.Y. and T.E.M. acknowledge support from the NSF under Grant DMR-1952877. Y.K.S., M.J.H., and A.C.T.v.D. acknowledge support from the project sponsored by the Army Research Laboratory under Cooperative Agreement W911NF-12-2-0023.

1. J. M. Tarascon, M. Armand, Issues and challenges facing rechargeable lithium batteries. *Nature* **414**, 359–367 (2001).
2. J. W. Choi, D. Aurbach, Promise and reality of post-lithium-ion batteries with high energy densities. *Nat. Rev. Mater.* **1**, 16013 (2016).
3. H. Kim *et al.*, Metallic anodes for next generation secondary batteries. *Chem. Soc. Rev.* **42**, 9011–9034 (2013).
4. W. Xu *et al.*, Lithium metal anodes for rechargeable batteries. *Energy Environ. Sci.* **7**, 513–537 (2014).
5. D. Lin, Y. Liu, Y. Cui, Reviving the lithium metal anode for high-energy batteries. *Nat. Nanotechnol.* **12**, 194–206 (2017).
6. X. B. Cheng, R. Zhang, C. Z. Zhao, Q. Zhang, Toward safe lithium metal anode in rechargeable batteries: A review. *Chem. Rev.* **117**, 10403–10473 (2017).
7. K. Yan *et al.*, Selective deposition and stable encapsulation of lithium through heterogeneous seeded growth. *Nat. Energy* **1**, 16010 (2016).
8. E. Peled, S. Menkin, Review—SEI: Past, present and future. *J. Electrochem. Soc.* **164**, A1703–A1719 (2017).
9. S. Wei, S. Choudhury, Z. Tu, K. Zhang, L. A. Archer, Electrochemical interphases for high-energy storage using reactive metal anodes. *Acc. Chem. Res.* **51**, 80–88 (2018).
10. S. Li *et al.*, Developing high-performance lithium metal anode in liquid electrolytes: Challenges and progress. *Adv. Mater.* **30**, e1706375 (2018).
11. D. Aurbach, Review of selected electrode-solution interactions which determine the performance of Li and Li ion batteries. *J. Power Sources* **89**, 206–218 (2000).
12. Y. Gao *et al.*, Salt-based organic-inorganic nanocomposites: Towards A stable lithium metal/Li_{10} GeP_2 S_{12} solid electrolyte interface. *Angew. Chem. Int. Ed. Engl.* **57**, 13608–13612 (2018).
13. Y. Gao *et al.*, Polymer-inorganic solid-electrolyte interphase for stable lithium metal batteries under lean electrolyte conditions. *Nat. Mater.* **18**, 384–389 (2019).
14. N.-W. Li, Y.-X. Yin, C.-P. Yang, Y.-G. Guo, An artificial solid electrolyte interphase layer for stable lithium metal anodes. *Adv. Mater.* **28**, 1853–1858 (2016).
15. Z. Tu *et al.*, Designing artificial solid-electrolyte interphases for single-ion and high-efficiency transport in batteries. *Joule* **1**, 394–406 (2017).
16. X. Liang *et al.*, A facile surface chemistry route to a stabilized lithium metal anode. *Nat. Energy* **6**, 17119 (2017).
17. Y. Gao *et al.*, Interfacial chemistry regulation via a Skin-grafting strategy enables high-performance lithium-metal batteries. *J. Am. Chem. Soc.* **139**, 15288–15291 (2017).
18. J. Qian *et al.*, High rate and stable cycling of lithium metal anode. *Nat. Commun.* **6**, 6362 (2015).
19. Y. Lu, K. Korf, Y. Kambe, Z. Tu, L. A. Archer, Ionic-liquid-nanoparticle hybrid electrolytes: Applications in lithium metal batteries. *Angew. Chem. Int. Ed. Engl.* **53**, 488–492 (2014).
20. L. Suo *et al.*, Fluorine-donating electrolytes enable highly reversible 5-V-class Li metal batteries. *Proc. Natl. Acad. Sci. U.S.A.* **115**, 1156–1161 (2018).

21. X. Fan *et al*., Non-flammable electrolyte enables Li-metal batteries with aggressive cathode chemistries. *Nat. Nanotechnol.* **13**, 715–722 (2018).
22. S. Chen *et al*., High-voltage lithium-metal batteries enabled by localized high-concentration electrolytes. *Adv. Mater.* **30**, e1706102 (2018).
23. S. Jiao *et al*., Stable cycling of high-voltage lithium metal batteries in ether electrolytes. *Nat. Energy* **3**, 1–8 (2018).
24. C. Z. Zhao *et al*., An anion-immobilized composite electrolyte for dendrite-free lithium metal anodes. *Proc. Natl. Acad. Sci. U.S.A.* **114**, 11069–11074 (2017).
25. H. Zhang *et al*., Electrolyte additives for lithium metal anodes and rechargeable lithium metal batteries: Progress and perspectives. *Angew. Chem. Int. Ed. Engl.* **57**, 15002–15027 (2018).
26. G. Salitra *et al*., High-performance cells containing lithium metal anodes, $LiNi_{0.6}Co_{0.2}Mn_{0.2}O_2$ (NCM 622) cathodes, and fluoroethylene carbonate-based electrolyte solution with practical loading. *ACS Appl. Mater. Interfaces* **10**, 19773–19782 (2018).
27. Y. Lu, Z. Tu, L. A. Archer, Stable lithium electrodeposition in liquid and nanoporous solid electrolytes. *Nat. Mater.* **13**, 961–969 (2014).
28. I. A. Shkrob, T. W. Marin, Y. Zhu, D. P. Abraham, Why bis(fluorosulfonyl)imide is a "magic anion" for electrochemistry. *J. Phys. Chem. C* **118**, 19661–19671 (2014).
29. S. Choudhury *et al*., Confining electrodeposition of metals in structured electrolytes. *Proc. Natl. Acad. Sci. U.S.A.* **115**, 6620–6625 (2018).
30. S. Chen *et al*., Functional organosulfide electrolyte promotes an alternate reaction pathway to achieve high performance in lithium-Sulfur batteries. *Angew. Chem. Int. Ed. Engl.* **55**, 4231–4235 (2016).
31. R. Khurana, J. L. Schaefer, L. A. Archer, G. W. Coates, Suppression of lithium dendrite growth using cross-linked polyethylene/poly(ethylene oxide) electrolytes: A new approach for practical lithium-metal polymer batteries. *J. Am. Chem. Soc.* **136**, 7395–7402 (2014).
32. S.-O. Tung, S. Ho, M. Yang, R. Zhang, N. A. Kotov, A dendrite-suppressing composite ion conductor from aramid nanofibres. *Nat. Commun.* **6**, 6152 (2015).
33. K. Liu *et al*., Lithium metal anodes with an adaptive "solid-liquid" interfacial protective layer. *J. Am. Chem. Soc.* **139**, 4815–4820 (2017).
34. J. Lopez *et al*., Effects of polymer coatings on electrodeposited lithium metal. *J. Am. Chem. Soc.* **140**, 11735–11744 (2018).
35. R. Mukherjee *et al*., Defect-induced plating of lithium metal within porous graphene networks. *Nat. Commun.* **5**, 3710 (2014).
36. C.-P. Yang, Y.-X. Yin, S.-F. Zhang, N.-W. Li, Y.-G. Guo, Accommodating lithium into 3D current collectors with a submicron skeleton towards long-life lithium metal anodes. *Nat. Commun.* **6**, 8058 (2015).
37. D. Lin *et al*., Three-dimensional stable lithium metal anode with nanoscale lithium islands embedded in ionically conductive solid matrix. *Proc. Natl. Acad. Sci. U.S.A.* **114**, 4613–4618 (2017).
38. Y. Zhang *et al*., High-capacity, low-tortuosity, and channel-guided lithium metal anode. *Proc. Natl. Acad. Sci. U.S.A.* **114**, 3584–3589 (2017).
39. T. Wang, R. Villegas Salvatierra, A. S. Jalilov, J. Tian, J. M. Tour, Ultrafast charging high capacity asphalt-lithium metal batteries. *ACS Nano* **11**, 10761–10767 (2017).
40. Z. Liang *et al*., Composite lithium metal anode by melt infusion of lithium into a 3D conducting scaffold with lithiophilic coating. *Proc. Natl. Acad. Sci. U.S.A.* **113**, 2862–2867 (2016).
41. H. Ye *et al*., Stable Li plating/stripping electrochemistry realized by a hybrid Li reservoir in spherical carbon granules with 3D conducting skeletons. *J. Am. Chem. Soc.* **139**, 5916–5922 (2017).
42. G. Li *et al*., Stable metal battery anodes enabled by polyethylenimine sponge hosts by way of electrokinetic effects. *Nat. Energy* **3**, 1076–1083 (2018).
43. R. Zhang *et al*., Lithiophilic sites in doped graphene guide uniform lithium nucleation for dendrite-free lithium metal anodes. *Angew. Chem. Int. Ed. Engl.* **56**, 7764–7768 (2017).
44. F. Shi *et al*., Lithium metal stripping beneath the solid electrolyte interphase. *Proc. Natl. Acad. Sci. U.S.A.* **115**, 8529–8534 (2018).
45. Z. Han *et al*., Ammonia solution strengthened three-dimensional macro-porous graphene aerogel. *Nanoscale* **5**, 5462–5467 (2013).
46. E. Bekyarova *et al*., Chemical modification of epitaxial graphene: Spontaneous grafting of aryl groups. *J. Am. Chem. Soc.* **131**, 1336–1337 (2009).
47. J. A. Belmont, R. M. Amici, C. P. Galloway, "Reaction of carbon black with diazonium salts, resultant carbon black products and their uses" U.S. Patent No. 7, 294, 185 (2017).
48. S. S. Zhang, K. Xu, J. L. Allen, T. R. Jow, Effect of propylene carbonate on the low temperature performance of Li-ion cells. *J. Power Sources* **110**, 216–221 (2002).
49. S. Tippmann, D. Walper, L. Balboa, B. Spier, W. G. Bessler, Low-temperature charging of lithium-ion cells part I: Electrochemical modeling and experimental investigation of degradation behavior. *J. Power Sources* **252**, 305–316 (2014).
50. F. Wang *et al*., Chemical distribution and bonding of lithium in intercalated graphite: Identification with optimized electron energy loss spectroscopy. *ACS Nano* **5**, 1190–1197 (2011).
51. Y. Gao *et al*., General method of manipulating formation, composition, and morphology of solid-electrolyte interphases for stable Li-alloy anodes. *J. Am. Chem. Soc.* **139**, 17359–17367 (2017).
52. S. S. Zhang, K. Xu, T. R. Jow, A new approach toward improved low temperature performance of Li-ion battery. *Electrochem. Commun.* **4**, 928–932 (2002).
53. G. Kresse, J. Furthmüller, Efficient iterative schemes for ab initio total-energy calculations using a plane-wave basis set. *Phys. Rev. B Condens. Matter* **54**, 11169–11186 (1996).
54. P. E. Blöchl, Projector augmented-wave method. *Phys. Rev. B Condens. Matter* **50**, 17953–17979 (1994).
55. J. P. Perdew, K. Burke, M. Ernzerhof, Generalized gradient approximation made simple. *Phys. Rev. Lett.* **77**, 3865–3868 (1996).
56. S. Grimme, J. Antony, S. Ehrlich, H. Krieg, A consistent and accurate ab initio parametrization of density functional dispersion correction (DFT-D) for the 94 elements H-Pu. *J. Chem. Phys.* **132**, 154104 (2010).